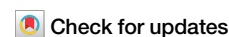


<https://doi.org/10.1038/s42005-024-01721-7>

Carrier transport mechanisms of titanium nitride and titanium oxynitride electron-selective contact in silicon heterojunction solar cells



Chenxi Liu, Yang Wang, Jinpei Liu, Runze Ma, Hao Liu, Qi Wang , Yujun Fu, Qiming Liu & Deyan He

It is widely accepted that an effective carrier-selective contact is indispensable for high performance crystalline silicon (c-Si) solar cells. However, the properties of these carrier-selective contact materials significantly differ from c-Si in terms of band gap, work function, lattice constant. Consequently, this gives rise to challenges such as band discontinuity and suspended bonds at the interface, which subsequently impact the specific carrier transport process and potentially lead to a reduction primarily in the fill factor at the device level. Titanium nitride (TiN) and titanium oxynitride (TiO_xN_y) have been employed as an electron-selective contact in both c-Si and perovskite solar cells, demonstrating their effectiveness in enhancing the performance of these devices. Based on the detailed characterizations of the band alignment, the carrier transport mechanisms are analyzed using multiple models, and the theoretical results are basically self-consistent through the verification of variable temperature experiments. These analytical methods can also provide solutions for analyzing the band structure and transport mechanism of diverse heterojunctions, ultimately contributing to the design and optimization of semiconductor heterojunction devices.

Along with the increasing demands for clean energy in the global energy market, photovoltaic (PV) technology which converts solar energy into electric energy, plays a more and more important role. The wafer-based crystalline silicon PV technology dominates the world PV market which has made up over 95% market share in 2023¹. The power conversion efficiency (PCE) of the traditional c-Si solar cell based on diffused *p-n* junction is largely limited by the high carrier recombination velocity at the metal-silicon contact regions. As c-Si and metal contact directly, metal may induce large density of electronic states near the interface within the band gap of silicon, resulting in more than 50% recombination losses in high efficiency c-Si solar cells². Besides, in order to overcome Fermi level pinning (FLP) to get an ohmic contact between the metal electrode and c-Si, a widely used method is inserting a heavily doped polysilicon (poly-Si) layer between c-Si and metal^{3–5}. But heavy doping also induces Auger recombination, bandgap narrowing and free carrier absorption in c-Si, limiting the further improvement of the device performance⁶. In recent years, a lot of carrier-selective passivating contact technologies have been explored successfully. With the electron-selective TiO_2 and hole-selective $\text{NiO}_x/\text{MnO}_x$ bilayer, the PCEs of 22.1% and 21.6% have been achieved, respectively^{7,8}.

However, these carrier-selective passivating contact materials usually exhibit a significant difference in band gap compared to c-Si, leading to a pronounced discontinuity in the band structure at the heterojunction interface. The emergence of “spikes” or “cliffs” at various positions plays a crucial role in determining potential barriers encountered during carrier transport processes. Even within the heterojunction formed by identical material, different material conditions (such as varying annealing temperatures and durations) can induce some subtle changes in the band structure, which significantly impact the current transport characteristics and ultimately lead to undesirable device performance degradation. Heterojunction structures are widely employed not only in solar cells but also in various specialized semiconductor devices, where their unique band alignments and transport characteristics are critical. For example, by arranging proper band alignment, a considerably large injection ratio can be achieved to realize population inversion condition required for heterojunction laser; the suitable heterojunction doping profile and band alignment give rise to extremely high electron mobilities by creating a two-dimensional electron gas within a dopant-free region, which is utilized in high electron mobility transistor (HEMT)^{9,10}. Therefore, in order to further optimize the structures

School of Materials and Energy, LONGi Institute of Future Technology, Lanzhou University, Lanzhou 730000, China. e-mail: liuqm@lzu.edu.cn

of solar cells and other heterojunction devices, it is necessary to conduct basic research that determines the band alignment and carrier transport mechanism of specific heterojunction.

The physical conditions of heterojunction interfaces are inherently complicated. The practical heterojunction interface is not strictly abrupt, there might be atomic reconfiguration and a dipole layer between the interface. In experiment, accurately determining valence band offset (VBO) and conduction band offset (CBO) poses challenges, because the measurement error associated with electron affinity is often substantial. Besides, due to lattice mismatch and imperfection of growth technology, there are always some interface states which can act as recombination centers, generating recombination currents within space charge regions. These states can also turn into intermediate states of multi-step tunneling, in some cases, they can even dominate the overall transport process¹¹. In addition, the space charge region of an isotype heterojunction consists of an accumulation layer on one side and a depletion layer on the other. Considering the spatial variation of the band on the accumulation side, the contribution of free carriers to the overall charge distribution cannot be ignored, thereby rendering the solution of Poisson equation considerably challenging. These factors present difficulties in determining the band alignment and analyzing the carrier transport process. Recent years, several studies have been conducted, including experimental and numerical approaches, but a number of issues remain unclarified, and some of the results are contradictory^{11–15}.

Because of its exceptional thermal and chemical stability, as well as its quasi-metallic conductivity, titanium nitride has already been used as a gate electrode for field effect transistors and memory devices in the semiconductor industry and functioning as a capacitor electrode and copper diffusion barrier in interconnect technology. Recent years, there have also been several reports on applications of TiN or TiO_xN_y to c-Si and perovskite solar cells^{16–18}. In this work, we fabricate silicon-organic hybrid heterojunction solar cells incorporating either as-deposited TiN or annealed TiN (TiO_xN_y) electron-selective contacts, and determine relatively precise band alignments by measuring the VBO and CBO of heterojunction interfaces. Basing on these results, the carrier transport equations of the heterojunction are deduced in detail using diffusion and thermal emission theory respectively. Finally, the basic self-consistent results are obtained by comparing the theoretical results with the experimental results at varying temperatures, which enables us to deduce the most probable mechanism governing carrier transport in various conditions.

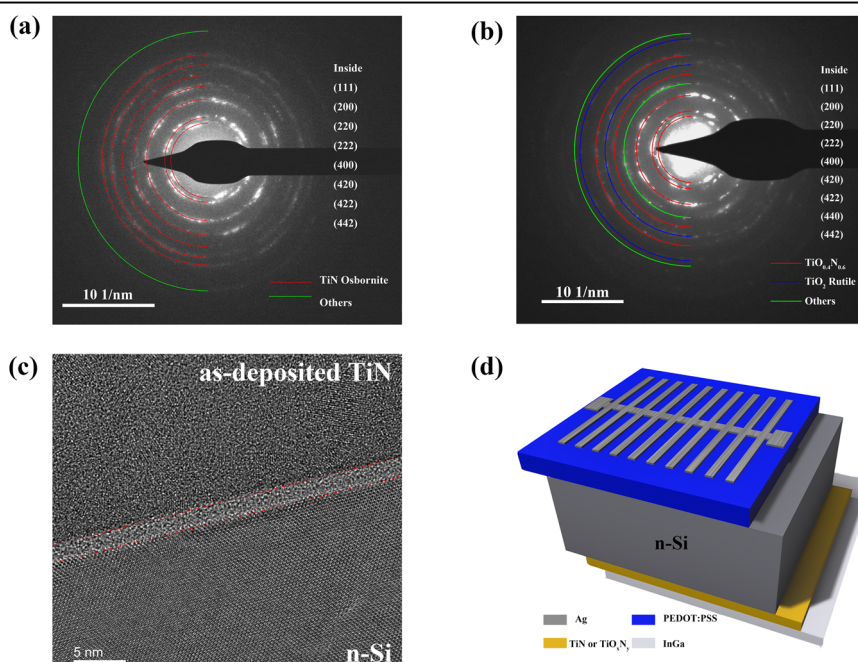
Results and discussion

The as-deposited TiN films are prepared via magnetron sputtering, while the TiO_xN_y films are obtained by oxidizing sputtered TiN films using a controlled annealing temperature in an oxygen atmosphere (details are provided in Methods). To understand physical properties of as-deposited and annealed films, high-resolution transmission electron microscopy (TEM) have been conducted. Figure 1c shows that the as-deposited film is polycrystalline where amorphous contrast along with a distribution of crystalline particles, and the sizes of those particles ranging from 5 nm to 20 nm (more TEM images about the interface topography can be seen in Supplementary Fig. S4). It is worth noting that there is a distinct contrast layer of approximately 2 nm between the *n*-Si and as-deposited TiN interface, we consider it to be the amorphous mixture of Ti-N-Si formed spontaneously during the deposition process, similar amorphous mixture has been reported in the sputtering of some other materials¹⁹. The detailed calculation procedure of diffraction patterns is given in Supplementary Table S1–S3. Figure 1a show that the as-deposited film can be assigned to the cubic phase of TiN Osbornite, while the annealed film forms a mixture of TiN Osbornite, TiO , TiO_2 Rutile and $\text{TiO}_{0.4}\text{N}_{0.6}$ phase (Fig. 1b and Supplementary Table S3).

To verify the effectiveness of as-deposited TiN and annealed TiN (TiO_xN_y) as an electron-conductive, hole-blocking contact, we prepare a solution-process hybrid heterojunction solar cell with a simple structure using TiN or TiO_xN_y as a full-area back contact (Fig. 1d). The main Photovoltaic parameters of the hybrid solar cells with different thickness of as-deposited TiN films are listed in Supplementary Table S4 and Supplementary Fig. S2. By inserting a 30 nm TiN layer, the short-circuit current exhibits an increase from 24.72 mA cm^{-2} to 28.20 mA cm^{-2} , accompanied by an enhancement in the PCE. Similar improvements can also be seen in previous studies^{17,20}. However, the PCE of those hybrid solar cells incorporating annealed TiN (TiO_xN_y) is almost zero, whereas the sheet resistances and minority carrier lifetime of annealed films barely change (Supplementary Table S5 and Supplementary Fig. S5). This substantial disparity can be attributed to the fundamental modification in band alignment of heterojunction formed by TiO_xN_y /*n*-Si, more details will be provided below.

Since the positions of potential “spikes” and “cliffs” can have great influence on carrier transport process, the accurate determinations of VBO and CBO are crucial. Generally, electron affinity χ and band gap E_g are used

Fig. 1 | Crystal phase composition of TiN and TiO_xN_y . **a, b** Diffraction patterns of as-deposited TiN and annealed TiN (TiO_xN_y), respectively. Different colored rings represent different crystal phase. **c** Cross-sectional transmission electron microscopy (TEM) images of as-deposited TiN/*n*-Si interface. **d** The schematic of poly(3,4-ethylenedioxythiophene):poly(styrene sulfonate) (PEDOT:PSS)/*n*-Si hybrid heterojunction solar cell with a full-area TiN or TiO_xN_y rear electron-selective contact.



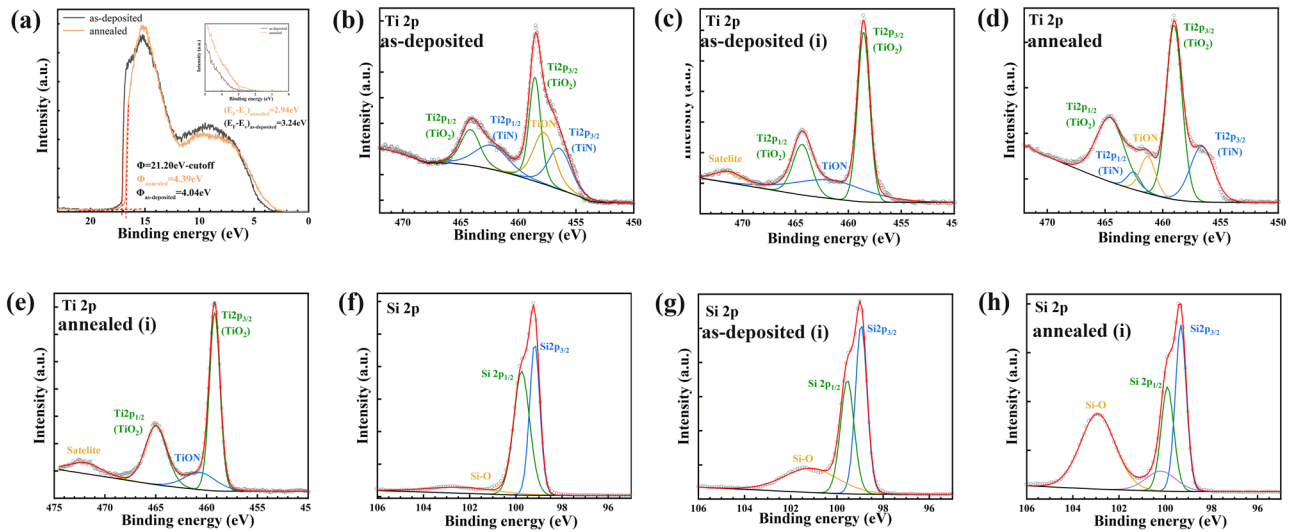


Fig. 2 | Characterization of heterojunction band offsets. **a** The ultraviolet photoelectron spectroscopy (UPS) spectra of TiN and TiO_xN_y . **b–e** X-ray photoelectron spectroscopy (XPS) spectra of Ti 2p. **f–h** XPS spectra of Si 2p. Note that the hollow circle data points in (**b**) to (**h**) represent the raw data, while the red curves represent

envelope curves. The blue, green and yellow curves represent the peaks of different components. Spectra marked with “(i)” are determined from the structure of 2 nmTiN/ TiO_xN_y /200 μmSi , which characterize the chemical states of the interface.

to estimate VBO and CBO (Anderson’s rule):

$$\Delta E_c = \chi_1 - \chi_2 \quad (1)$$

$$\Delta E_v = \Delta E_g - \Delta E_c \quad (2)$$

However, the electron affinity with local vacuum energy as reference is highly susceptible to the material surface condition. Moreover, in terms of device design, VBO and CBO are best accurate to the order of kT (~ 0.026 eV), whereas electron affinity is usually a large energy (typically 4–5 eV). Consequently, even a minor measurement error in electron affinity can have an unacceptable impact on VBO and CBO values.

In this study, detailed high-resolution X-ray photoelectron spectroscopy (XPS) and ultraviolet photoelectron spectroscopy (UPS) analysis are conducted to determine the relatively accurate band offsets of TiN/ n -Si and TiO_xN_y / n -Si heterojunctions. We prepare three structures: (1) 50nmTiN (or TiO_xN_y)/200 μmSi is used for measuring the binding energy from the core levels (CL) and valence band maxima (VBM) of TiN or TiO_xN_y ; (2) 2 nmTiN (or TiO_xN_y)/200 μmSi is used for measuring CL binding energy of TiN, TiO_xN_y and Si at the interface; (3) 200 μmSi without the top TiN or TiO_xN_y layer is used for measuring the CL binding energy and VBM of Si. The VBO value can be calculated by the Kraut’s method^{19,21–23}:

$$\Delta E_v = (E_{CL}^{Si} - E_{VBM}^{Si}) - (E_{CL}^{TiN} - E_{VBM}^{TiN}) + (E_{CL}^{TiN}(i) - E_{CL}^{Si}(i)) \quad (3)$$

where E_{CL}^{Si} and E_{CL}^{TiN} are the CL binding energies of Si and TiN (or TiO_xN_y) from the structure 50nmTiN (or TiO_xN_y)/200 μmSi , respectively. For Si, the $\text{Si}2p_{3/2}$ peak is used in the calculation; for TiN and TiO_xN_y , the $\text{Ti}2p_{3/2}$ (TiO_2 component) is selected. $E_{CL}^{Si}(i)$ and $E_{CL}^{TiN}(i)$ are the CL binding energy of Si and TiN (or TiO_xN_y) measured from the structure of 2 nmTiN (or TiO_xN_y)/200 μmSi , respectively. E_{VBM}^{TiN} is obtained from the cutoff in UPS spectrum. Once the VBO is obtained, the CBO can be calculated by:

$$\Delta E_c = \Delta E_v + E_g^{Si} - E_g^{TiN} \quad (4)$$

where E_g^{Si} and E_g^{TiN} are band gap of Si and TiN, respectively. We use the optical band gap values extracted via ultraviolet-visible (UV-vis) spectroscopy by Tauc’s method (see Supplementary Fig. S6)^{17,24}. The optical band gap of c -Si is determined to be 1.08 eV, the widely accepted band gap value of c -Si is 1.12 eV. Therefore, in this calculation, we adopt the median value

(1.10 eV) as a compromise. The optical band gap value of TiN is determined to be 3.20 eV, which is consistent with the previous study^{17,18}.

Figure 2 display the XPS and UPS results of TiN and TiO_xN_y films. Since thinner films are more sensitive to oxidation, spectra obtained from the 2 nmTiN/200 μmSi structure exhibit a high proportion of TiO_2 component, which is caused by the inevitable oxidation during both fabrication and testing processes. As shown in Fig. 2a, the work function of as-deposited TiN film is determined to be 4.04 eV, while the work function of annealed film becomes 4.39 eV. During annealing, the addition of oxygen to TiN results in a reduction in the proportion of N element (acting as a donor), leading to a decrease in the relative position of the Fermi level which represents the electron filling degree within the system. Consequently, this causes the increase in the work function. The VBM of n -Si is calculated by the doping concentration and band gap. According to the resistivity-doping concentration diagram of silicon at 300 K²⁵, the n -Si used in this study, with a resistivity of 1–3 $\Omega\text{-cm}$, exhibits a doping concentration of approximately $2.5 \times 10^{15} \text{ cm}^{-3}$. The calculation results show that the phosphorus doped n -Si with concentration of $3 \times 10^{17} \text{ cm}^{-3}$ is ionized about 90% at 300 K, therefore $2.5 \times 10^{15} \text{ cm}^{-3}$ is a fairly low concentration, we can consider it to be completely ionized at room temperature, i.e., the equilibrium electron concentration n_0 equal to the doping concentration N_D and satisfy the Boltzmann distribution function (non-degenerate state). By employing Eq. (5), the computed VBM of n -Si is 0.86 eV (N_c is the effective state density of conduction band, for n -Si, N_c is about $2.8 \times 10^{19} \text{ cm}^{-3}$ at 300 K).

$$E_F - E_c = kT \ln \left(\frac{N_D}{N_c} \right) = 0.026 \text{ eV} \times \ln \left(\frac{2.5 \times 10^{15}}{2.8 \times 10^{19}} \right) = -0.242 \text{ eV} \quad (5)$$

The CL binding energies obtained from fitted high-resolution XPS peak positions, VBM obtained from the cutoff in UPS spectrum, the calculation results of VBO and CBO according to Eqs. (3) and (4) are summarized in Table 1.

Based on these results, we constructed band alignments for the two different heterojunctions under equilibrium condition which is shown in Fig. 3. We adopt 4.05 eV and 4.25 eV as the reference electron affinity values for n -Si and TiO_xN_y , respectively^{14,17,26,27}. Although these two values are very rough, they do not influence the overall band alignment, since the band offsets have been calibrated by the above test results. Now we can discuss the

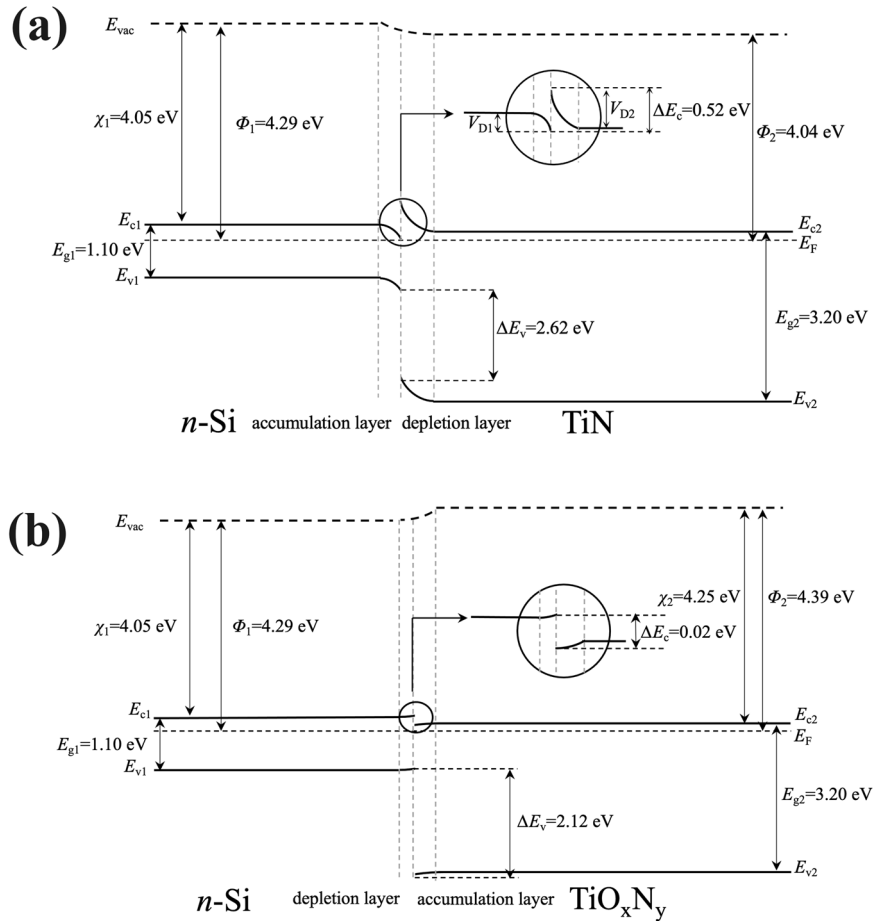
Table 1 | The measured parameters required for the calculation of band offsets

	As-deposited	Annealed		As-deposited	Annealed
$E_{2p_{3/2}}^{TiN}$ (eV)	458.56	459.02	E_{VBM}^{Si}	0.86	~
$E_{2p_{1/2}}^{TiN}$ (eV)	464.14	464.55	$E_{2p_{3/2}}^{Si}$ (eV)	99.19	~
$E_{2p_{3/2}}^{TiN}$ (i) (eV)	458.56	459.20	$E_{2p_{3/2}}^{Si}$ (i) (eV)	98.95	99.33
$E_{2p_{1/2}}^{TiN}$ (i) (eV)	464.37	464.98	ΔE_v (eV)	2.62	2.12
E_{VBM}^{TiN} (eV)	3.24	2.94	ΔE_c (eV)	0.52	0.02

Summary of core level (CL) binding energies, valence band maxima (VBM), conduction band offset and valence band offset. “2p1/2” and “2p3/2” represent the spin-orbit splitting peaks of 2p spectra. “(i)” represents the binding energy measured from the structure of 2nmTiN (or TiO_xN_y)/200 μ mSi.

Fig. 3 | The band alignments of the heterojunctions under equilibrium condition.

a Heterojunction formed by *n*-Si and as-deposited TiN. **b** Heterojunction formed by *n*-Si and annealed TiN (TiO_xN_y). Φ is the work function; E_F is the Fermi level; E_c is the bottom of conduction band and E_v is the top of valence band. The disparity in the work functions of TiN and TiO_xN_y results in a reversal of the direction of the built-in electric field.



specific carrier transport process based on the band alignments. Let us commence by examining the heterojunction formed by as-deposited TiN/*n*-Si (Fig. 3a). The current equations are deduced by using diffusion theory and thermal electron emission theory, respectively. All derivations are based on the following assumptions: (1) The system is under equilibrium condition. (2) The temperature is sufficiently high, and the concentration of injected non-equilibrium carrier is low, allowing for simplification of Fermi-Dirac distribution to Boltzmann distribution (nondegenerate state). (3) The junction is assumed to be abrupt, neglecting any generated or recombination currents in the space charge region. Definitions of all symbols are listed in Table 2.

Assuming the interface is located at coordinate $x = 0$, when a forward voltage (with negative voltage on TiN side) is applied to the junction, we can define the boundaries of space charge region as $x = -x_1$ (*n*-Si side), and $x = x_2$ (TiN side). In equilibrium state, the continuity equation satisfied by the *n*-Si

side is:

$$D_{n1} \frac{\partial^2 n_1}{\partial x^2} + \mu_{n1} E \frac{\partial n_1}{\partial x} + \mu_{n1} n_1 \frac{\partial E}{\partial x} - \frac{\Delta n_1}{\tau_{n1}} = 0 \quad (6)$$

In case of low applied voltage, term $\frac{\partial E}{\partial x}$ is small and can be neglected. However, due to the accumulation layer on the *n*-Si side, the electric field in diffusion region isn't strictly zero (discussion of the potential distribution in the accumulation layer can be found in Supplementary Note S2), for simplicity and to focus solely on our main objective, we will disregard this complexity as well as any other external influences, so that:

$$D_{n1} \frac{\partial^2 n_1}{\partial x^2} - \frac{\Delta n_1}{\tau_{n1}} = 0 \quad (7)$$

Table 2 | The notation for each variable or constant

Variable (constant)	Interpretation	Variable (constant)	Interpretation
Subscript 1	Physical quantity of <i>n</i> -Si	τ_n and τ_p	Carrier lifetime
Subscript 2	Physical quantity of TiN or TiO _x N _y	q	Electronic charge
χ	Electron affinity	L_n and L_p	Carrier diffusion length
E_g	Band gap	V	Applied voltage
E_c and E_v	Bottom of conduction band and top of valence band, respectively	V_1 and V_2	The applied voltage drops in the <i>n</i> -Si and TiN (or TiO _x N _y), respectively
E_F	Fermi level	β	Ideal factor
E_{vac}	Vacuum level	$f_B(E)$	Boltzmann distribution function
Φ	Work function	$g_c(E)$	State density function of conduction band bottom
k	Boltzmann constant	m_n^*	Effective mass of electron
T	Absolute temperature	\hbar	Reduced Planck constant
ΔE_c	Conduction band offset (CBO)	R_{sh}	Shunt resistance
ΔE_v	Valence band offset (VBO)	R	Series resistance
N_D	Doping concentration of <i>n</i> -Si	I_s	Saturation current of the junction
N_c	Effective state density of conduction band	v_{x10} and v_{x20}	The minimum thermal velocity required for an electron to cross a potential barrier
N_v	Effective state density of valence band	V_D	Built-in voltage
n and p	Electron and hole concentration	gp	The change in the number of electrons per unit volume at unit time due to external factors (e.g., incident light)
n_0 and p_0	Equilibrium electron and hole concentration, respectively (non-degenerate state)	dn	The number of electrons per unit volume between energy intervals dE or velocity interval dv
Δn and Δp	Excess electron and hole concentration, respectively	A^*	Effective Richardson constant
μ_n and μ_p	Carrier mobility	ϵ	Dielectric constant
E	Electric field intensity	\sinh	Hyperbolic sine function
D_n and D_p	Electron and hole diffusion coefficient, respectively	a	Absorbance of materials

The general solution is:

$$\Delta n_1(x) = n_1(x) - n_{10} = A \exp\left(\frac{-x}{L_{n1}}\right) + B \exp\left(\frac{x}{L_{n1}}\right) \quad (8)$$

As shown in Fig. 3a, in thermal equilibrium, the boundary conditions of electron are:

$$n_1(-x_1) = n_{20} \exp\left[-\frac{q(V_{D2} - V_2)}{kT}\right] = n_{10} \exp\left(\frac{qV_2}{kT}\right) \quad (9-a)$$

$$n_1(-\infty) = n_{10} = n_{20} \exp\left(-\frac{qV_{D2}}{kT}\right) \quad (9-b)$$

By Substituting Eq. (9-a) and Eq. (9-b) into Eq. (8), we obtain:

$$\Delta n_1(x) = n_1(x) - n_{10} = n_{10} \left[\exp\left(\frac{qV_2}{kT}\right) - 1 \right] \exp\left(\frac{x_1 + x}{L_{n1}}\right) \quad (10)$$

The current density of electron diffusion is determined:

$$J_{n,2 \rightarrow 1}|_{x=-x_1} = qD_{n1} \frac{d(\Delta n_1(x))}{dx} \Big|_{x=-x_1} = \frac{qD_{n1}n_{10}}{L_{n1}} \left[\exp\left(\frac{qV_2}{kT}\right) - 1 \right] \exp\left(\frac{x_1 + x}{L_{n1}}\right) \Big|_{x=-x_1} = \frac{qD_{n1}n_{10}}{L_{n1}} \left[\exp\left(\frac{qV_2}{kT}\right) - 1 \right] \quad (11)$$

Similarly, the equilibrium condition of the hole is:

$$p(x_2) = p_{10} \exp\left[-\frac{q(V_D + \Delta E_v - V)}{kT}\right] = p_{20} \exp\left(\frac{qV}{kT}\right) \quad (12)$$

where $V = V_1 + V_2$, $V_D = V_{D1} + V_{D2}$, the hole and total diffusion current density is:

$$J_{p,1 \rightarrow 2}|_{x=x_2} = qD_{p2} \frac{d(\Delta p_2(x))}{dx} \Big|_{x=x_2} = \frac{qD_{p2}p_{20}}{L_{p2}} \left[\exp\left(\frac{qV}{kT}\right) - 1 \right] \exp\left(\frac{x_2 - x}{L_{p2}}\right) \Big|_{x=x_2} = \frac{qD_{p2}p_{20}}{L_{p2}} \left[\exp\left(\frac{qV}{kT}\right) - 1 \right] \quad (13)$$

$$J_{total} = J_{n,2 \rightarrow 1}|_{x=-x_1} + J_{p,1 \rightarrow 2}|_{x=x_2} = \frac{qD_{n1}n_{10}}{L_{n1}} \left[\exp\left(\frac{qV_2}{kT}\right) - 1 \right] + \frac{qD_{p2}p_{20}}{L_{p2}} \left[\exp\left(\frac{qV}{kT}\right) - 1 \right] \quad (14)$$

Note that $p_{20} \ll n_{10}$, the total current density can be simplified as:

$$J_{total} = \frac{qD_{n1}n_{10}}{L_{n1}} \left[\exp\left(\frac{qV_2}{kT}\right) - 1 \right] = \frac{qD_{n1}n_{10}}{L_{n1}} \left[\exp\left(\frac{qV}{\beta kT}\right) - 1 \right] \quad (15)$$

where β is the ideal factor derived from diffusion theory, it represents the proportion of the total forward voltage falling on the depletion region of the as-deposited TiN side.

Then we derive the current equation of the as-deposited heterojunction based on thermal emission theory, which is a distinct model. The detailed derivation process is given in the Supplementary Note S1, while we present only the principal results here. As shown in Fig. 3a, the height of the barrier that an

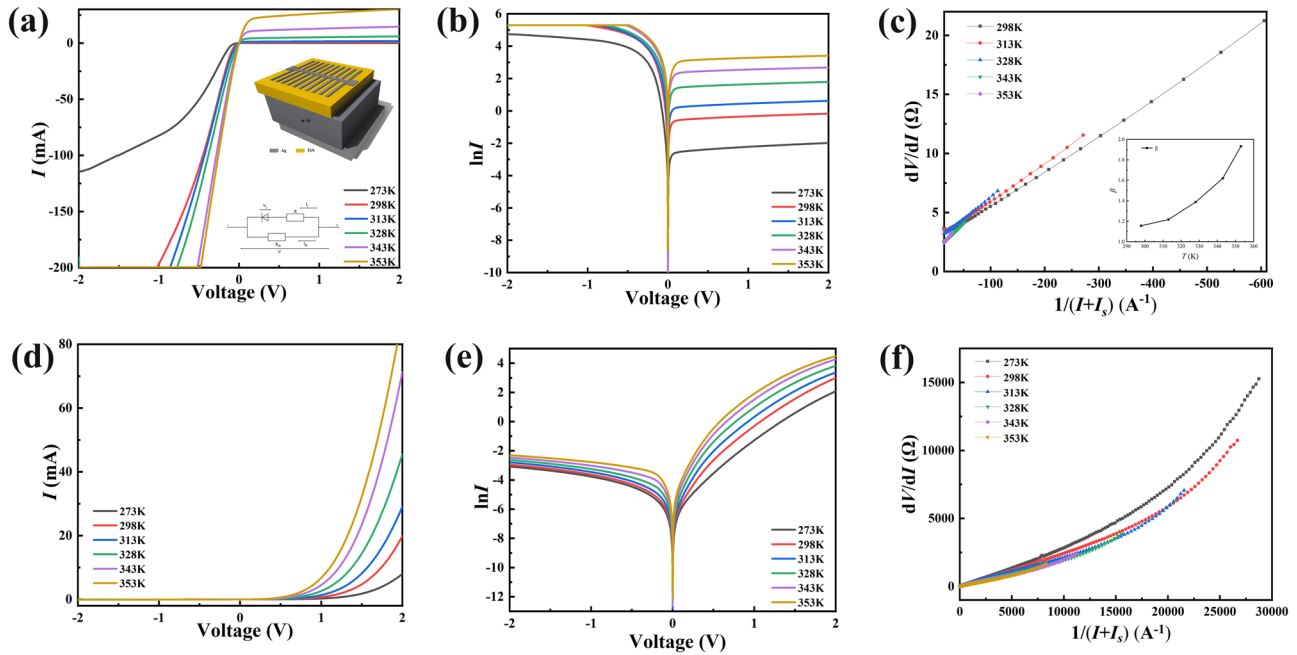


Fig. 4 | Dark current-voltage characteristics of heterojunctions at various temperatures. **a, b** Dark current-voltage characteristics, equivalent circuit diagram, structure schematic of the heterojunction formed by as-deposited TiN and *n*-Si under different temperatures (± 200 mA is the clamp current for the test instrument, the positive electrode is connected to the Ag electrode on the TiN or TiO_xN_y side). **d, e** Dark current-voltage characteristics of heterojunction formed by TiO_xN_y and *n*-

Si. **c** The as-deposited heterojunction $dV/dI-1/(I+I_s)$ characteristics under forward bias (The inserted picture is the ideal factor for different temperatures calculated from the slope). **f** $dV/dI-1/(I+I_s)$ characteristics of annealed heterojunction under forward bias. The various colors correspond to the characteristic curves observed at varying temperatures.

electron needs to cross from left (*n*-Si) to right (as-deposited TiN) is $\Delta E_c - q(V_{D1} - V_1)$, and the height from right to left is $q(V_{D2} - V_2)$, the total current density is:

$$J_{total} = qn_{10} \left(\frac{kT}{2\pi m_{n2}^*} \right)^{\frac{1}{2}} \exp \left(\frac{qV_2}{kT} \right) - qn_{10} \left(\frac{kT}{2\pi m_{n1}^*} \right)^{\frac{1}{2}} \exp \left[-\frac{\Delta E_c - q(V_{D1} - V_1)}{kT} \right] \quad (16)$$

Note that:

$$\exp \left(-\frac{\Delta E_c - q(V_{D1} - V_1)}{kT} \right) \ll \exp \left(\frac{qV_2}{kT} \right) \quad (17)$$

Therefore, the total current density can be simplified as:

$$J_{total} = qn_{10} \left(\frac{kT}{2\pi m_{n2}^*} \right)^{\frac{1}{2}} \exp \left(\frac{qV_2}{kT} \right) = qn_{10} \left(\frac{kT}{2\pi m_{n2}^*} \right)^{\frac{1}{2}} \exp \left(\frac{qV}{\beta' kT} \right) \quad (18)$$

where β' is the ideal factor derived from emission theory. The above derivation reveals that the ideal factor of a heterojunction, which signifies the deviation of junction current from $\exp(qV/kT)$, is often determined by the potential barriers that carriers must traverse. The potential barriers are dictated by the unique band alignments. It should be noted that not all heterojunctions exhibit meaningful ideal factors. For instance, if the approximation of Eq. (17) no longer valid, according to Eq. (16), the emission theory suggests that the heterojunction lacks favorable rectification characteristics, and thus renders discussion of an ideal factor impractical. However, in the TiN/*n*-Si heterojunction, it is evident from Fig. 3a that ΔE_c significantly surpasses V_{D1} , thus confirming the validity of this approximation. Apparently, β' equal to β . Although the starting point of the two theories are completely different, they ultimately converge to a common ideal factor through appropriate reduction. While the saturation currents of

the two theories are quite different. The relationship between saturation current and temperature dominated by diffusion mechanism is related to specific carrier scattering mechanism, but in general, change of saturation current with temperature is considerably less drastic than that in emission mechanism (Eq. (S13) in Supplementary Note S1). Therefore, we carry out variable temperature *I*-*V* tests for the heterojunctions, calculate and analyze the change of ideal factor with temperature experimentally.

The device structure and equivalent circuit used for variable temperature *I*-*V* tests are shown in Fig. 4a. From the equivalent circuit diagram, the *I*-*V* equation is obtained:

$$I = \frac{V}{R_{sh}} + I_s \left[\exp \left(\frac{qV_j}{\beta kT} \right) - 1 \right] = \frac{V}{R_{sh}} + I_s \left\{ \exp \left[\frac{q \left(V - \left(I - \frac{V}{R_{sh}} \right) R \right)}{\beta kT} \right] - 1 \right\} \quad (19)$$

Rearrange the equation and take the derivative of *V* with respect to *I*:

$$V = \frac{1}{1 + \frac{R}{R_{sh}}} \left[IR + \frac{\beta kT}{q} \ln \left(\frac{I}{I_s} + 1 - \frac{V}{I_s R_{sh}} \right) \right] \quad (20)$$

$$\frac{dV}{dI} = \frac{R + \frac{\beta kT}{q} \left(\frac{1}{I + I_s - V/R_{sh}} \right)}{1 + \frac{R}{R_{sh}} + \frac{\beta kT}{q} \left[\frac{1}{(I + I_s) R_{sh} + V} \right]} \quad (21)$$

Usually R_{sh} is large, so the above equation can be simplified to:

$$\frac{dV}{dI} = R + \frac{\beta kT}{q} \left(\frac{1}{I + I_s} \right) \quad (22)$$

Thereupon, we can calculate the ideal factor at different temperature from the slope of the $dV/dI-1/(I+I_s)$ curves. Since the actual heterojunction does not exhibit strict saturation under inverse bias conditions, we take the current at the reverse voltage of -1 V as the saturation current I_s . The potential impact of Schottky junctions resulting from the contact between the metal electrode and material is discussed in Supplementary Note S3.

As depicted in Fig. 4a, the heterojunction formed by as-deposited TiN and *n*-Si exhibits obvious rectification characteristic. When the TiN side is subjected to a negative voltage, the heterojunction is in a forward conduction state (i.e., forward bias), which aligns with our previous presented band alignment in Fig. 3a. The $dV/dI-1/(I+I_s)$ curves demonstrate satisfactory linearity at different temperatures, expect for the curve at 273 K. Note that the number of data points varies across different temperatures, because the current reaches the clamp current of the instrument faster at higher temperatures, and these data should be discarded. The I - V curve exhibits anomalous behavior at lower temperature (273 K), showing that at higher forward bias, currents and voltages are no longer exponentially related, and appear to be linear, i.e., resistance property. This deviation could be attributed to the presence of a small potential well at the heterojunction interface. As shown in Fig. 3a, when the negative voltage is applied to TiN side, electrons migrate from the *n*-Si side to the TiN side, with some being trapped within the potential well due to the discontinuity of the conduction band. The accumulation of these electrons within the potential well impedes further electron injection and reduction of the built-in barrier, which is manifested in the case of low temperature. Similar phenomena have been previously reported in $\text{Al}_{0.35}\text{Ga}_{0.65}\text{As}/\text{GaAs}$ *Np*-type heterojunctions²⁸.

Figure 4c shows that the ideal factor of the as-deposited heterojunction increases with temperature. The rigorous verification of this experimental result should be carried out by solving the numerical solution of Eq. (S24-a) (see Supplementary Note S2) at different temperatures, but here we provide a qualitative explanation utilizing the depletion layer approximation: without considering the free carrier concentration on the charge distribution, Eq. (23) is easily derived by solving the Poisson equation:

$$\frac{V_{D1} - V_1}{V_{D2} - V_2} = \frac{\epsilon_2 N_{D2}}{\epsilon_1 N_{D1}} \quad (23)$$

As discussed previously, the doping concentration of *n*-Si $N_{D1} = 2.5 \times 10^{15} \text{ cm}^{-3}$, which is considered to be completely ionized at room temperature, while the ionization rate of TiN will increase with the increase of temperature. Therefore, according to Eq. (23), the proportion of the total forward voltage falling on the TiN side decreases, since $\beta = V/V_2$ (Eqs. (15) and (18)), the ideal factor increases with temperature. The experimental and theoretical results for as-deposited heterojunction are consistent.

As shown in Fig. 4a, the reverse saturation currents of as-deposited heterojunction exhibit significant variations with temperature, indicating that the carrier transport mechanism is dominated by the thermal electron emission. Although there exist several other mechanisms which we have not discussed in detail due to their minimal disparity in equation forms. Tunneling through barrier satisfies the form of Eq. (24) in general²⁹:

$$J = J_s \exp(AV) \quad (24)$$

where J_s is weakly dependent on temperature, and the constant A is independent of temperature but dependent on the shape of the barrier. Because only electrons with higher energy can reach the bottom of the barrier and subsequently tunnel through the barrier, the tunneling mechanism is usually in series with the emission mechanism, resulting in a turning point commonly observed in the $\ln I$ - V curves. However, none of these features align with our experimental results.

In the case of high interfacial state density at certain isotype heterojunction interfaces, the tunneling process can also be a multi-step process through the interfacial state within the band gap. The resulting current equation resembles Eq. (24), with the exception that the saturation current is related to the interfacial state density³⁰. It has been reported that when there

are a huge number of interfacial states between the heterojunction interfaces, the current characteristics are similar to those of two Schottky diodes in reverse series, satisfying Eq. (25) and exhibiting bidirectional saturation characteristics^{31,32}. However, this phenomenon was not observed in our experimental results. Therefore, we conclude that the dominant transport mechanism of as-deposited TiN/*n*-Si heterojunction is the thermal electron emission.

$$J = \frac{-2J_{s1}J_{s2}\sinh(qV/2kT)}{J_{s1}\exp(qV/2kT) + J_{s2}\exp(-qV/2kT)} \quad (25)$$

As shown in Fig. 4d, the heterojunction formed by TiO_xN_y and *n*-Si also exhibits distinct rectification characteristics, while the external voltage that makes it forward biased is opposite of the as-deposited heterojunction. This is caused by the disparity in the work function of TiN and TiO_xN_y , resulting in a reversal of the built-in field at the heterojunction, as depicted in Fig. 3. Notably, Fig. 4f shows that the $dV/dI-1/(I+I_s)$ curves at various temperatures deviate linearity, suggesting that either the annealed heterojunction fails to comply with the equivalent circuit described by Eq. (19), or that the shunt resistance R_{sh} is insufficiently large enough to simplify Eq. (21) to Eq. (22). From the perspective of band structure, as shown in Fig. 3b, the potential barriers for electrons and holes need to cross are almost zero when the TiO_xN_y /*n*-Si heterojunction is forward biased. Furthermore, the *n*-Si side has depletion layer of electrons and the relative positioning of the conduction band of *n*-Si is higher than that of TiO_xN_y , which lead to the fact that the carrier transport can no longer be solved by thermal equilibrium state but should be considered from the perspective of “extraction” regardless of diffusion or thermal emission models. Hence, when the applied electric field pulls out all electrons near the depletion layer, it may also lead to deviation from the ideal model.

So far, we have not found a satisfactory model that can experimentally extract the ideal factor of the annealed heterojunction from the variable temperature I - V curves. However, upon comparing the I - V curves of as-deposited and annealed heterojunctions, it is obvious that the inverse saturation currents of the annealed heterojunction exhibit much lower dependence on temperature. Therefore, based on the previous discussion, we speculate that the carrier transport mechanism of the annealed junction is diffusion, tunneling, or the combination of them. However, Fig. 3b qualitatively illustrates a relatively low conduction band barrier in annealed heterojunction. Unless there is substantial number of interface states within the band gap, such a small barrier is unlikely to impede electron transport, so we tend to consider that the dominant transport mechanism is diffusion.

Conclusion

In summary, by using the results from UPS and XPS characterizations, we calibrate the accurate band structure of the heterojunction formed by TiN/*n*-Si and TiO_xN_y /*n*-Si, respectively. By employing certain approximations, we calculated the current equations of heterojunction under ideal condition based on diffusion and emission theory. Furthermore, through a comparison between the variable temperature tests and theoretical results, we determine that the dominant carrier transport mechanism of TiN/*n*-Si heterojunction is governed by thermal emission. Additionally, we provide an explanation for why there is an increase in the ideal factor with temperature. We have encountered challenges in extracting the ideal factor of TiO_xN_y /*n*-Si heterojunction experimentally, perhaps because some approximations are no longer valid, or a new model needs to be established. As discussed in Supplementary Note S2, a more accurate physical model should be based on the analysis of the electric field within the accumulation layer. However, through qualitative analysis we propose that the diffusion mechanism likely governs the transport process of annealed heterojunction. We believe that the analytical methods presented in this study are also applicable to other heterojunctions and can contribute to the design and optimization of various semiconductor devices such as SHJ solar cells, field effect transistors and memory devices that utilize the unique characteristics of heterojunctions.

Methods

Titanium nitride and titanium oxynitride films deposition and characterization: The as-deposited titanium nitride films were deposited on the pre-cleaned *n*-Si by radiofrequency magnetron sputtering at 75 W and 20 sccm argon gas using a titanium nitride target (purity of 99.9%) under a pressure of 0.95–1.0 Pa. Before deposition, we conducted pre-sputter the target for 3 minutes to clean the potential dirt and natural oxide layer on the target. The titanium oxynitride films were fabricated by annealing as-deposited titanium nitride films at 450 °C for 2 hours in a tube furnace in an atmosphere of argon mixed with trace amount of oxygen. The rate of heating and cooling in annealing process is 5 °C per minute.

The cross-sectional images, elemental distribution and diffraction patterns were obtained by high-resolution TEM (Titan Themes Cubed G2 300). To meet TEM testing requirements, all samples were thinned to dimensions of 6 μm × 4 μm × 100 nm prior to the testing.

XPS and UPS spectra were carried out by two different machines (Kratos AXIS Ultra DLD and Axis Supra), with a monochromatic Al Kα (1486.6 eV) X-ray source for XPS and a He-I excitation (21.2 eV) for UPS. XPS spectra were analyzed by using a commercially available software CasaXPS, C 1 s peak at 284.8 eV was used to calibrate the binding energy. For the analysis of Ti 2p spectra, the basic rules we follow as below: (1) Ti 2p spectra have obvious spin-orbit splitting peaks (Ti 2p_{1/2} and Ti 2p_{3/2}). (2) The difference of the splitting peaks is various in different chemical states, in nitride state the difference is about 6.0 eV, in oxide state the difference is about 5.7 eV. (3) The full width at half maxima (FWHM) of the splitting peaks are roughly the same in most cases, but since the peak of Ti 2p_{1/2} is usually much wider than that of Ti 2p_{3/2}, the peak height of Ti 2p_{1/2} is lower than Ti 2p_{3/2}. Note that the TiO₂ component of Ti 2p_{1/2} and Ti 2p_{3/2} peak were clearly observed in as-deposited sample, which indicated the presence of a significant amount of oxygen even in as-deposited TiN films. This might be caused by oxidation from residual oxygen in the sputtering chamber or during the storage and testing process. Besides, the XPS test is sensitive to the surface of samples (usually 1 ~ 10 nm), so even if the oxidation is shallow, it's still easy to be detected. Similar phenomenon is also reported in previous research¹⁶. For the analysis of Si 2p, we follow the rule below: spectra of crystalline silicon have spin-orbit splitting peaks (Si 2p_{1/2} and Si 2p_{3/2}) with a difference about 0.63 eV, which giving asymmetric peak shape.

Silicon solar cells Fabrication: Double-side polished phosphorus doped *n*-type monocrystalline silicon wafers were used for device preparation (1–3 Ω·cm, 200 ± 10 μm, (100)). The silver electrodes (purity of 99.999%) used in both the variable temperature tests and solar cell tests were deposited by thermal evaporation. An aqueous solution of poly(3,4-ethylenedioxythiophene):poly(styrene sulfonate) (PEDOT:PSS) were prepared on base of 7 wt.% ethylene glycol and 93 wt.% Clevious PH 1000. To enhance the adhesion between the aqueous PEDOT:PSS solution and the substrate, a drop of the surfactant Triton X-100 is added. The resulting aqueous solution is stirred with a magnetic stirrer for 8 h to achieve homogeneity and stability before application. The PEDOT:PSS solution was dropped onto the wafer and spin coated at 2000 rpm for 60 s, followed by annealing at 120 °C for 15 min. The silver electrodes (purity of 99.999%) used in both the variable temperature tests and solar cell tests were deposited by thermal evaporation. The active area of cells is 1 cm².

Reporting summary

Further information on research design is available in the Nature Portfolio Reporting Summary linked to this article.

Data availability

The data are available from the corresponding author on reasonable request.

Received: 2 March 2024; Accepted: 27 June 2024;

Published online: 06 July 2024

References

- Jäger-Waldau, A. Snapshot of photovoltaics. *EPJ Photovolt.* **14**, 23 (2023).
- Benick, J. et al. High efficiency *n*-type Si solar cells on Al₂O₃-passivated boron emitters. *Appl. Phys. Lett.* **92**, 253504 (2008).
- Ullah, H. et al. Crystalline silicon (c-Si)-based tunnel oxide passivated contact (TOPCon) solar cells: A review. *Energies* **16**, 715 (2023).
- Kafle, B. et al. TOPCon-technology options for cost efficient industrial manufacturing. *Sol. Energy Mater. Sol. Cells* **227**, 111100 (2021).
- Green, M. A. The passivated emitter and rear cell (PERC): From conception to mass production. *Sol. Energy Mater. Sol. Cells* **143**, 190–197 (2015).
- Allen, T. G., Bullock, J., Yang, X., Javey, A. & De Wolf, S. Passivating contacts for crystalline silicon solar cells. *Nat. Energy* **4**, 914–928 (2019).
- Yang, X., Weber, K., Hameiri, Z. & De Wolf, S. Industrially feasible, dopant-free, carrier-selective contacts for high-efficiency silicon solar cells. *Prog. Photovoltaics: Res. Appl.* **25**, 896–904 (2017).
- Li, L. et al. NiO_x/MoO_x bilayer as an efficient hole-selective contact in crystalline silicon solar cells. *Cell Rep. Phys. Sci.* **2**, 100684 (2021).
- Cheung, D. T. & Pearson, G. L. An analysis of the superinjection phenomenon in heterostructure devices. *J. Appl. Phys.* **46**, 2313–2314 (1975).
- Dingle, R., Stormer, H. L., Gossard, A. C. & Wiegmann, W. Electron mobilities in modulation-doped semiconductor heterojunction superlattices. *Appl. Phys. Lett.* **33**, 665–667 (1978).
- Dao, V.-A. et al. Carrier transport mechanisms of reactively direct current magnetron sputtered tungsten oxide/*n*-type crystalline silicon heterojunction. *J. Power Sources* **472**, 228460 (2020).
- Luo, Y. et al. Carrier transport enhancement mechanism in highly efficient antimony selenide thin-film solar cell. *Adv. Funct. Mater.* **33**, 2213941 (2023).
- Liu, C. et al. Band gap and defect engineering for high-performance cadmium-free Sb₂(S,Se)₃ solar cells and modules. *Adv. Funct. Mater.* **32**, 2209601 (2022).
- Ozel, K. & Yildiz, A. The potential barrier-dependent carrier transport mechanism in *n*-SnO₂/*p*-Si heterojunctions. *Sens. Actuators A: Phys.* **332**, 113141 (2021).
- Gerling, L. G. et al. Transition metal oxides as hole-selective contacts in silicon heterojunctions solar cells. *Sol. Energy Mater. Sol. Cells* **145**, 109–115 (2016).
- Yang, X. et al. Dual-function electron-conductive, hole-blocking titanium nitride contacts for efficient silicon solar cells. *Joule* **3**, 1314–1327 (2019).
- Yang, X. et al. A highly conductive titanium oxynitride electron-selective contact for efficient photovoltaic devices. *Adv. Mater.* **32**, e2002608 (2020).
- Peng, J. et al. Centimetre-scale perovskite solar cells with fill factors of more than 86 per cent. *Nature* **601**, 573–578 (2022).
- Zhu, Y. et al. X-ray photoelectron spectroscopy analysis and band offset determination of CeO₂ deposited on epitaxial (100), (110), and (111) Ge. *J. Vac. Sci. Technol.* **32**, 011217 (2014).
- Yu, J. et al. Titanium nitride electron-conductive contact for silicon solar cells by radio frequency sputtering from a TiN target. *ACS Appl. Mater. Interfaces* **12**, 26177–26183 (2020).
- Kraut, E. A., Grant, R. W., Waldrop, J. R. & Kowalczyk, S. P. Precise determination of the valence-band edge in X-ray photoemission spectra: application to measurement of semiconductor interface potentials. *Phys. Rev. Lett.* **44**, 1620–1623 (1980).
- Chen, X. et al. Modification of band offsets of InGaZnO₄/Si heterojunction through nitrogenation treatment. *J. Alloy. Compd.* **647**, 1035–1039 (2015).
- Wang, J. et al. Band offsets of epitaxial Tm₂O₃ high-*k* dielectric films on Si substrates by X-ray photoelectron spectroscopy. *Appl. Surf. Sci.* **258**, 6107–6110 (2012).

24. Tauc, J., Grigorovici, R. & Vancu, A. Optical properties and electronic structure of amorphous germanium. *Phys. Status Solidi (b)* **15**, 627–637 (1966).
25. Irvin, J. C. Resistivity of bulk silicon and of diffused layers in silicon. *Bell Syst. Tech. J.* **41**, 387–410 (1962).
26. Ozel, K. & Yildiz, A. A Self-Powered Ultraviolet Photodetector with Ultrahigh Photoresponsivity (208mA W^{-1}) based on SnO_2 Nanostructures/Si Heterojunctions. *Phys. Status Solidi (RRL) – Rapid Res. Lett.* **15** (2021).
27. Ozel, K. & Yildiz, A. High-detectivity ultraviolet-B photodetector based on SnO_2 thin film/Si heterojunction. *Semicond. Sci. Technol.* **36**, 095001 (2021).
28. Wu, C. M. & Yang, E. S. Current suppression induced by conduction-band discontinuity in $\text{Al}_{0.35}\text{Ga}_{0.65}\text{As}$ -GaAs N-p heterojunction diodes. *J. Appl. Phys.* **51**, 2261–2263 (1980).
29. Rediker, R., Stopek, S. & Ward, J. Interface-alloy epitaxial heterojunctions. *Solid-State Electron.* **7**, 621–622 (1964).
30. Riben, A., Donnelly, J. & Feucht, D. Electrical characteristics of Ge-GaAs and Ge-Si p-n heterojunctions. *IEEE Trans. Electron Devices* **12**, 511–511 (1965).
31. Van Opdorp, C. & Kanerva, H. Current-voltage characteristics and capacitance of isotype heterojunctions. *Solid-State Electron.* **10**, 401–421 (1967).
32. Oldham, W. & Milnes, A. Interface states in abrupt semiconductor heterojunctions. *Solid-State Electron.* **7**, 153–165 (1964).

Acknowledgements

This work was supported by the National Natural Science Foundation of China (grant nos. 61804070), the Science and Technology Projects of Gansu Province (no. 21JR7RA467), and the Fundamental Research Funds for the Central Universities (grant nos. Izujbky-2023-14 and Izujbky-2022-it30).

Author contributions

C.L.: designed experiments and analyzed the results; wrote the paper. Q.L.: revised and edited the paper; Funding acquisition. Y.W.: conceived the idea. J. L.: conducted TEM tests. R.M. and H.L.: discussed the results. Q.W. and Y.F.: Equipment instructions. D.H.: Funding acquisition.

Competing interests

The authors declare no competing interests.

Additional information

Supplementary information The online version contains supplementary material available at <https://doi.org/10.1038/s42005-024-01721-7>.

Correspondence and requests for materials should be addressed to Qiming Liu.

Peer review information *Communications Physics* thanks Abdullah Yildiz and the other, anonymous, reviewer(s) for their contribution to the peer review of this work. A peer review file is available.

Reprints and permissions information is available at <http://www.nature.com/reprints>

Publisher's note Springer Nature remains neutral with regard to jurisdictional claims in published maps and institutional affiliations.

Open Access This article is licensed under a Creative Commons Attribution 4.0 International License, which permits use, sharing, adaptation, distribution and reproduction in any medium or format, as long as you give appropriate credit to the original author(s) and the source, provide a link to the Creative Commons licence, and indicate if changes were made. The images or other third party material in this article are included in the article's Creative Commons licence, unless indicated otherwise in a credit line to the material. If material is not included in the article's Creative Commons licence and your intended use is not permitted by statutory regulation or exceeds the permitted use, you will need to obtain permission directly from the copyright holder. To view a copy of this licence, visit <http://creativecommons.org/licenses/by/4.0/>.

© The Author(s) 2024